Earth and Planetary Science Letters 511 (2019) 141–153

Contents lists available at ScienceDirect

Earth and Planetary Science Letters

www.elsevier.com/locate/epsl

# Divergent Mediterranean seawater circulation during Holocene sapropel formation – Reconstructed using Nd isotopes in fish debris and foraminifera

Jiawang Wu [a,b,*], Katharina Pahnke [c], Philipp Böning [c], Li Wu [a], Annie Michard [d], Gert J. de Lange [a,b]

[a] State Key Laboratory of Marine Geology, Tongji University, Siping 1239, 200092 Shanghai, China
[b] Department of Earth Sciences – Geochemistry, Faculty of Geosciences, Utrecht University, Princetonplein 9, 3584 CC Utrecht, the Netherlands
[c] Max Planck Research Group for Marine Isotope Geochemistry, Institute for Chemistry and Biology of the Marine Environment (ICBM), University of Oldenburg, Carl-von-Ossietzky-Strasse 9-11, 26129 Oldenburg, Germany
[d] CEREGE, Aix-Marseille Université, CNRS, IRD, CEREGE UM34, 13545 Aix en Provence, France

ARTICLE INFO

*Article history:*
Received 14 October 2018
Received in revised form 12 January 2019
Accepted 19 January 2019
Available online 6 February 2019
Editor: D. Vance

*Keywords:*
Nd isotopes
sapropel S1
Mediterranean thermohaline circulation
$\varepsilon_{Nd}$ modeling
fish debris/teeth

ABSTRACT

The recurrent deposition of organic-rich sapropel layers in the eastern Mediterranean Sea (EMS) has been attributed to deep-water stagnation and enhanced biological production. However, the underlying climatic interactions, paleoceanographic processes, and associated ventilation dynamics are still debated. Here, we present a basin-wide reconstruction of circulation systematics during sapropel S1 formation (~10.8–6.1 kyr BP), using the Nd isotope composition ($\varepsilon_{Nd}$) as paleo-seawater tracer. Our $\varepsilon_{Nd}$ data from fish debris and foraminifera tests are remarkably radiogenic compared to today, and spatially and temporally constant. These results predominantly reflect enhanced Nile versus Atlantic contributions, and indicate that EMS deep-water stagnation prevailed below ~800 m water-depth during S1 formation. Additional $\varepsilon_{Nd}$ records obtained from bulk sediment leachates show that such stagnation was preconditioned thousand(s) of years prior to S1 initiation by intensified Nile flooding, whereas it terminated with a basin-wide, deep-water renewal. In addition, decoupling of deep waters between the EMS and western Mediterranean Sea (WMS) is evident for the S1-period. Using a box-model for Nd in the EMS, the observed $\varepsilon_{Nd}$ distribution can be most adequately explained by a 2-fold increase in Nile discharge, and a 50% decrease in the EMS–WMS exchange that was mostly limited to the surface waters alone. The corresponding circulation during S1 was more sluggish and shallow for the EMS, but largely unaffected for the WMS. This implies that deep-water stagnation is a prerequisite for sapropel formation.


## 1. Introduction

### 1.1. Mediterranean circulation as related to sapropel formation

The semi-enclosed Mediterranean Sea has a thermohaline circulation, similar to that of the global ocean (Roether et al., 1996; Pinardi and Masetti, 2000). Driven by a negative freshwater balance, the anti-estuarine circulation transforms the surface inflow of relatively low-density Atlantic waters (i.e. Modified Atlantic Water, MAW) into deeper outflow of saltier intermediate water (i.e. Levantine Intermediate Water, LIW). Eastern Mediterranean Deep Water (EMDW) is formed regularly when sufficient cooling takes place in the mixture of surface water and LIW in the Adriatic and Aegean seas (Pinardi and Masetti, 2000) (Fig. 1). This circulation is highly sensitive to climate change, as witnessed by a recent shift in the deep-water formation (e.g. Roether et al., 1996). Variations in the Mediterranean circulation have been reported to play a role in the Atlantic Meridional Overturning Circulation (e.g. Jiménez-Espejo et al., 2015), and are closely linked to the repetitive occurrence of organic-rich sapropel layers in Mediterranean sediments (see review by Rohling et al., 2015). Sapropel formation has been attributed to stagnating deep-water conditions and increased biological production, as a result of enhanced freshwater and nutrient inputs during minima of the orbital precession cycle (Rossignol-Strick, 1983; Rohling, 1994; Emeis et al., 2000; De Lange et al., 2008; Schmiedl et al., 2010; Ziegler et al., 2010). However, many aspects of the complex interactions between climatic and paleoceanographic processes as

* Corresponding author at: State Key Laboratory of Marine Geology, Tongji University, Siping 1239, 200092 Shanghai, China.
*E-mail addresses:* jwwu@tongji.edu.cn, j.w.wu@uu.nl (J. Wu).

https://doi.org/10.1016/j.epsl.2019.01.036
0012-821X/

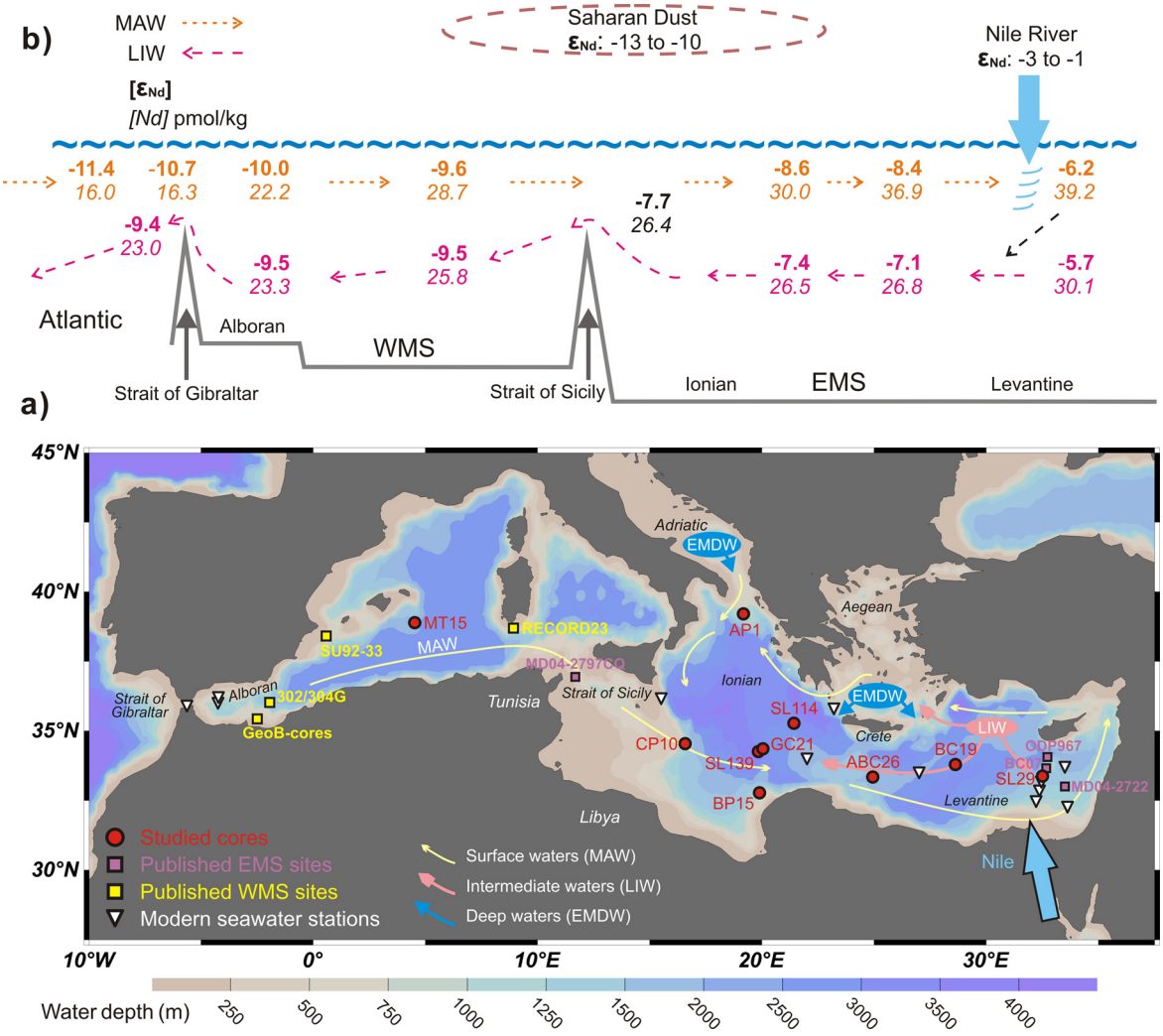


**Fig. 1.** a) Bathymetric map of the Mediterranean Sea showing the cores investigated in this study (red-circles: Table 1) and the sites of published data (EMS, purple-squares: Freydier et al., 2001; Scrivner et al., 2004; Cornuault et al., 2018; WMS, yellow-squares: Jiménez-Espejo et al., 2015; Dubois-Dauphin et al., 2017). Modern seawater stations are also indicated (white-triangles: Henry et al., 1994; Tachikawa et al., 2004; Vance et al., 2004). Generalized oceanography with Modified Atlantic Water (MAW), formation sites and pathways of Levantine Intermediate Water (LIW), and Eastern Mediterranean Deep Waters (EMDW) after Pinardi and Masetti (2000). b) A west–east transect summarizing the dissolved Nd concentration ([*Nd*] *italics*, in pmol/kg) and isotope composition ([$\varepsilon_{Nd}$] bold). Orange data and arrows represent the MAW (<200 m depth), whereas magenta indicate the LIW (200–800 m depth) (Spivack and Wasserburg, 1988; Henry et al., 1994; Tachikawa et al., 2004; Vance et al., 2004). Typical $\varepsilon_{Nd}$ signatures for Nile River (Scrivner et al., 2004; Wu et al., 2016) and Saharan Dust (Frost et al., 1986; Scheuvens et al., 2013) are also shown. (For interpretation of the colors in the figure(s), the reader is referred to the web version of this article.)

related to circulation dynamics and sapropel formation, are still highly debated.

The knowledge of sapropel formation is mostly based on the last, $^{14}$C-datable sapropel S1 (~10.8–6.1 kyr BP; after De Lange et al., 2008), coinciding with the most-recent African Humid Period. This sapropel was deposited in the eastern- (EMS) but not in the western-Mediterranean Sea (WMS). Surface-water freshening is thought to have inhibited deep-water formation, thereby preconditioning S1 formation, as evidenced by proxies of benthic foraminifera (Kuhnt et al., 2008; Schmiedl et al., 2010; Tesi et al., 2017) and redox-sensitive elements (Jilbert et al., 2010; Hennekam et al., 2014; Tachikawa et al., 2015; Matthews et al., 2017). Using planktonic foraminiferal $\delta^{18}$O to spatially estimate surface salinity changes and consequent circulation during S1; however, different hypotheses emerged: 1) a similar west–east gradient as today but weaker (Rohling and De Rijk, 1999; Emeis et al., 2000), 2) reversed to an estuarine-type pattern (Thunell and Williams, 1989), and 3) changed to a flat field, i.e. no gradient and not reversed (Kallel et al., 1997).

This discrepancy is mainly because of insufficient constraints on freshwater sources during sapropel formation. Physical-oceanography models have revealed that a higher freshwater input causes a stronger stagnation, yet that changes in the freshwater sources can modulate this effect (Myers et al., 1998; Myers, 2002). The astronomically induced freshwater forcing seems tightly correlated with the monsoon-related Nile flooding (Rossignol-Strick, 1983; Ziegler et al., 2010; Hennekam et al., 2014; Revel et al., 2015); while the reactivated North-African paleo-rivers and increased runoff from the northern borderlands could represent considerable inputs as well (Scrivner et al., 2004; Osborne et al., 2010; Filippidi et al., 2016; Wu et al., 2016, 2017; Tesi et al., 2017). A progressively increasing inflow of Atlantic waters was proposed to contribute to the initial onset of S1-related anoxia (Grimm et al., 2015). However, simulations of timing and extent for deep-water stagnation and sapropel deposition, and of related circulation changes in both EMS and WMS have yielded inconsistent – sometimes conflicting – results (Rohling, 1994; Myers et al., 1998; Stratford et al., 2000; Bianchi et al., 2006; Grimm et al., 2015; Cornuault et al., 2018).

All of these knowledge gaps strongly urge for a systematic reconstruction of the Mediterranean thermohaline circulation during the S1-period, based on water-mass properties rather than on indirectly derived parameters.

### 1.2. Nd isotopes as a water-mass tracer in Mediterranean archives

Neodymium isotope composition is conventionally expressed as: $\varepsilon_{Nd} = [(^{143}Nd/^{144}Nd)_{sample}/(^{143}Nd/^{144}Nd)_{CHUR} - 1] \times 10^4$, where CHUR (chondritic uniform reservoir) is 0.512638 (Jacobsen and Wasserburg, 1980). Seawater Nd isotopes have proven to be a quasi-conservative water mass proxy, thereby being a reliable tracer for ocean circulation (Tachikawa et al., 2017; and references therein). Commonly, observed dissolved $\varepsilon_{Nd}$ values originate from the mixing of water masses, while the interaction between dissolved and particulate phases may be considerable near continental margins (Lacan and Jeandel, 2005). In addition, particle scavenging was proposed to explain the decoupling of Nd concentrations and isotopes in the open ocean (Siddall et al., 2008).

In the modern Mediterranean, the dissolved $\varepsilon_{Nd}$ becomes increasingly radiogenic from west to east, with averaged water-column values ranging from ∼−11 to −8.5 in the WMS and ∼−7.5 to −5 in the EMS (Spivack and Wasserburg, 1988; Henry et al., 1994; Tachikawa et al., 2004; Vance et al., 2004). This gradient has been attributed to a mixing between the inflowing MAW (west-to-east: ∼−11.4 to −8.4) and the more radiogenic underlying LIW (east-to-west: ∼−5.7 to −9.4), which acquire their $\varepsilon_{Nd}$ signatures from the Atlantic water (∼−12 to −10) and the Nile discharge (∼−3 to −1), respectively (Fig. 1). Specifically, the partially dissolved Nile particles that mostly accumulate in the easternmost EMS, rather than the river water itself, were reported to be the dominant radiogenic Nd source (Tachikawa et al., 2004; Ayache et al., 2016). The fractional dissolution of Saharan dust ($\varepsilon_{Nd}$: ∼−13 to −10), the contributions of which are distributed uniformly over the EMS, is the major external source of unradiogenic Nd (Frost et al., 1986; Freydier et al., 2001; Tachikawa et al., 2004). The EMDW $\varepsilon_{Nd}$ composition is rather homogeneous, characterized by values of ∼−7.5 to −6.5 (Tachikawa et al., 2004).

Although the application of seawater $\varepsilon_{Nd}$ is particularly appropriate to study deep-water processes, to date, only a few Nd-related paleoceanography studies exist for the Mediterranean (Freydier et al., 2001; Scrivner et al., 2004; Osborne et al., 2010; Jiménez-Espejo et al., 2015; Dubois-Dauphin et al., 2017; Cornuault et al., 2018). This is probably because of the challenges to extract preserved $\varepsilon_{Nd}$ signals from reliable archives using appropriate approaches (cf. Tachikawa et al., 2014, 2017), especially for the sapropel-related periods characterized by redox-changing conditions.

Above all, biogenic apatite of fish debris/teeth has been recognized as the most reliable recorder of bottom-water $\varepsilon_{Nd}$ composition, even though its occurrence is not constant and barren samples are not uncommon (Martin and Scher, 2004; Martin et al., 2010; Horikawa et al., 2011; Tachikawa et al., 2014). During sapropel formation, fortunately, biogenic apatite may make up the bulk phosphorus inventory due to the anoxic bottom-water conditions (Schenau and De Lange, 2000; Slomp et al., 2002; Kraal et al., 2010). This allows a sufficient amount of fossil fish debris to be well preserved in un-oxidized sapropel S1 sections of some EMS cores (Slomp et al., 2002; De Lange et al., 2008).

The authigenic ferromanganese oxides precipitated in foraminiferal tests are also considered a generally robust archive (Roberts et al., 2012; Tachikawa et al., 2014; Wu et al., 2015; Blaser et al., 2016). However, there may be sedimentary environments under which the bottom-water $\varepsilon_{Nd}$ signature is not preserved by planktonic foraminifera (Roberts et al., 2012). Additionally, several attempts were made to extract the biogenic calcite $\varepsilon_{Nd}$ from cleaned planktonic foraminifera using oxidative-reductive leaching techniques, aiming to reflect changes in the EMS surface waters during sapropel times (e.g. Scrivner et al., 2004; Vance et al., 2004; Osborne et al., 2010).

However, recent studies have indicated that such oxidative-reductive cleaning cannot totally remove all of the authigenic Nd, because of the Nd concentration in the calcite lattice itself is orders of magnitude lower than in Fe–Mn oxides, causing indistinguishable $\varepsilon_{Nd}$ between cleaned and uncleaned foraminiferas (Roberts et al., 2012; Tachikawa et al., 2014; Wu et al., 2015). On the other hand, the fact that the predominance of authigenic Nd relative to biogenic Nd phases allows bulk carbonate fraction to be widely analyzed for Nd isotopes as a water-mass tracer (e.g. Freydier et al., 2001; Gourlan et al., 2008, 2010; Le Houedec et al., 2012, 2016). This is especially for pelagic, carbonate-rich sediments, due to the protective effect of carbonates during Nd extraction (cf. Blaser et al., 2016). It has been shown that carbonates act effectively as a buffer preventing acid-induced Nd mobilization from possible contaminations, such as volcanogenic matter, pre-formed continental Fe–Mn oxides, and labile detrital material (Wilson et al., 2013; Wu et al., 2015; Blaser et al., 2016).

Here, we present a basin-wide reconstruction of Mediterranean circulation patterns at the time of S1 formation, on the basis of bottom-water $\varepsilon_{Nd}$ data from 9 EMS cores (Table 1; Fig. 1). Our data are mainly derived from fish debris, and supplemented with those from foraminiferal tests (Table 2). Having a geographic and bathymetric coverage, these data allow us to constrain the changes in sources and mixing of water masses, driven by distinct deviations in the Mediterranean thermohaline circulation during the S1-period compared to the present-day. This is the first time that data for the deep-water proxy, $\varepsilon_{Nd}$ of fish debris, are reported for the Mediterranean Sea. In addition, data of bulk sediment leachates that have shown to be appropriate archives for paleo-seawater $\varepsilon_{Nd}$, are interpreted for 4 Mediterranean cores (Freydier et al., 2001; Tachikawa et al., 2004; Table 3). Furthermore, a box model is used to support more quantitative assessments of the Nd budget for the EMS (Fig. 5). All together these provide a solid basis to outline seawater-$\varepsilon_{Nd}$ changes and associated hydrological variations throughout the S1-equivalent period in the EMS and WMS.

## 2. Material and methods

### 2.1. Cores and chronologies

Nine cores with sapropel S1 layers are selected to give a geographic and bathymetric coverage of the EMS, plus one diagnostic core from the WMS (Table 1; Fig. 1). The age models for these cores are based on $^{14}C$ datings on planktonic foraminifera, and the well-established S1 boundaries as indicated by organic carbon, Ba/Al and Mn/Al (cf. De Lange et al., 2008). In terms of these sapropel indicators, all the EMS cores display differences between the early phase (S1a) and late phase (S1b) of sapropel S1, interrupted by the “8.2-kyr-BP event”. This widespread cooling event was recorded as a re-ventilation in the EMS, and sapropel deposition was generally more enhanced during early phase (cf. Rohling et al., 2015). For details see Supplementary information.

### 2.2. Nd isotope analyses

#### 2.2.1. Fish debris and foraminiferal tests

A total of 15 samples were handpicked from the >150-μm size fraction of wet-sieved sediments, and the analyses were done at ICBM, Oldenburg (Table 2).

Fish debris (∼0.2–2 mg), including teeth, bones, and fragments, were processed after Martin et al. (2010) using ultraclean reagents. Samples were ultrasonicated in methanol for 10 s, before pipetting

**Table 1**
General information of the investigated cores over the Mediterranean Sea.

| Site | Corer | Location | Water depth (m) | Cruise |
|---|---|---|---|---|
| CP10 | Box | 34°32.7′N, 16°34.0′E | 1501 | RV *Pelagia* 2011 |
| BP15 | Box | 32°46.7′N, 19°52.6′E | 665 | RV *Pelagia* 2001 |
| AP1 | Gravity | 39°13.0′N, 19°06.8′E | 811 | RV *Urania* 1998 |
| BC07 | Box | 33°40.0′N, 32°40.0′E | 893 | RV *Marion Dufresne* 1994/5 |
| GC21[a] | Gravity | 34°21.9′N, 20°02.1′E | 3250 | RV *Bannock* 1988 |
| SL139 | Box | 34°16.1′N, 19°49.8′E | 3293 | RV *Logachev* 1999 |
| SL114 | Box | 35°17.2′N, 21°24.5′E | 3390 | RV *Logachev* 1999 |
| ABC26 | Box | 33°21.3′N, 24°55.7′E | 2150 | RV *Tyro* 1987 |
| BC19 | Box | 33°47.9′N, 28°36.5′E | 2750 | RV *Marion Dufresne* 1991 |
| SL29 | Box | 33°23.4′N, 32°30.2′E | 1587 | RV *Logachev* 1999 |
| MT15[b] | Piston | 38°53.8′N, 04°30.6′E | 2373 | RV *Tyro* 1993 |

[a] Collected from a permanent anoxic, brine basin (Bannock Basin).
[b] Collected from the western Mediterranean Sea (WMS).

**Table 2**
Neodymium isotope composition of fish and foraminifera samples from the eastern Mediterranean Sea for the S1-period.

| Core | Depth (cm) | Age (cal. kyr BP) | Material[a] | $^{143}Nd/^{144}Nd$[b] | $\varepsilon_{Nd} \pm 2SD$[c] |
|---|---|---|---|---|---|
| CP10 | 20.5–21.5[d] | 6.1 | Fish | 0.512367 (15) | −5.3 ± 0.3 |
| CP10 | 24.5–25.0[d] | 7.2 | Fish | 0.512382 (22) | −5.0 ± 0.4 |
| CP10 | 26.0–26.5 | 7.5 | Fish | 0.512380 (12) | −5.0 ± 0.3 |
| CP10 | 28.0–28.5 | 7.8 | Fish | 0.512380 (12) | −5.0 ± 0.3 |
| CP10 | 30.0–30.5 | 8.3 | Fish | 0.512393 (10) | −4.8 ± 0.3 |
| CP10 | 34.5–35.0 | 9.6 | Fish | 0.512399 (15) | −4.7 ± 0.3 |
| BP15 | 32.5–33.0[e] | 8.8 | Foraminifera | 0.512324 (27) | −6.1 ± 0.5 |
| AP1 | 31.0–32.0 | 9.6 | Fish | 0.512389 (06) | −4.9 ± 0.3 |
| GC21 | 40.8[f] | 9.0 | Fish | 0.512375 (15) | −5.1 ± 0.3 |
| SL139 | 27.5–28.5[f] | 9.3 | Foraminifera | 0.512374 (05) | −5.2 ± 0.3 |
| SL114 | 32.75–34.25 | 9.6 | Fish | 0.512384 (19) | −5.0 ± 0.4 |
| ABC26 | 15.95–16.25[d] | 7.1 | Fish | 0.512384 (04) | −5.0 ± 0.3 |
| ABC26 | 20.45–20.75 | 8.9 | Fish | 0.512395 (10) | −4.8 ± 0.3 |
| BC19[g] | 24.5–27.5 | 9.3 | Foraminifera | 0.512406 (13) | −4.5 ± 0.3 |
| SL29 | 28.5–29.5 | 9.5 | Fish | 0.512398 (10) | −4.7 ± 0.3 |

[a] 0.2–2 mg of fish debris, including teeth, bones, and fragments; ∼30 mg of mixed planktonic foraminifera tests, predominance of *G. ruber*, with *G. sacculifer* & *G. bulloides* (see Section 2.2.1).
[b] Normalized to the JNdi-1 value of $^{143}Nd/^{144}Nd = 0.512115$ (Tanaka et al., 2000), with 2SD in brackets.
[c] Propagated errors, i.e. square root from the sum of squared internal and external errors.
[d] Samples taken from oxidized sapropel intervals.
[e] The relatively large error is due to the small amount of Nd that was analyzed, caused by its low concentration in foraminiferal calcite (Roberts et al., 2012).
[f] The same values from nearby cores but with different seafloor environments substantiate the bottom-water signatures of planktonic foraminifera in this study (see Section 3).
[g] Similar values from bulk sediment leachates are given (sample at 25.5–25.75 cm depth: −4.1 ± 0.3 $\varepsilon_{Nd}$; sample at 27–27.25 cm depth: −4.5 ± 0.3 $\varepsilon_{Nd}$; Table 3 and see also Supplementary information).

the fluids to waste. This step was subsequently applied in deionized water, and repeated until the water became clear and free of suspended particle. Potentially remaining detrital particles were checked under microscope and removed using an eyelash brush. Thereafter, the samples were leached in a closed Teflon beaker with 30% $H_2O_2$ at 80 °C for ∼2 min, dried down at 90 °C, followed by the digestion in a mixture of concentrated $HNO_3$ and HCl (1:1) at 140 °C for 4 min in open Teflon beakers.

For the cores where no fish debris was found, approximately 30 mg of mixed planktonic foraminifera (dominated by *G. ruber*, with *G. sacculifer* & *G. bulloides*) were used after the general protocols (Tachikawa et al., 2014; Wu et al., 2015). The shells were crushed between glass plates to open all chambers, and then ultrasonicated in deionized water for 2 min before pipetting off the supernatant. This step was repeated until the water remained clear and free of clay. The cleanliness was checked under microscope and any contaminant grains were removed. First, 0.5 ml of deionized water was added to cover the foraminiferal fragments; then the dissolution was performed using stepwise additions of 100 µl aliquots of 1 M acetic acid, until the reaction stopped.

Subsequently, all samples were purified by column chromatography. Rare earth elements (REE) were isolated using TRU-Spec columns, collected in 1 M HCl. Neodymium was then separated from other REE using Ln-Spec resin on volumetrically calibrated columns, with 0.25 M HCl as eluent (Wu et al., 2016). The Nd isotopes were analyzed using a Thermo Scientific® Neptune Plus multi-collector inductively coupled plasma mass spectrometer at ICBM. Instrumental mass bias was corrected by normalizing $^{146}Nd/^{144}Nd$ to 0.7219 using an exponential law. Measured $^{143}Nd/^{144}Nd$ ratios were normalized to the certified JNdi-1 value of 0.512115 (Tanaka et al., 2000). The 2SD external reproducibility based on analyses of JNdi-1 ($n = 17$) interspersed between the samples was better than 0.3 $\varepsilon_{Nd}$-units (Table 2). Blank levels were insignificant in all cases (<100 pg Nd).

### 2.2.2. Bulk sediment leachates

To reconstruct temporal changes across the S1-equivalent period, Nd isotope data of 4 cores along a west–east transect throughout the Mediterranean Sea are assembled and provided with new age models (Freydier et al., 2001; Tachikawa et al., 2004; Table 3). The analyses for these data were done on the authigenic/biogenic fraction of (∼100 mg) bulk sediment leached with (10 ml) 1 M HCl, thus including carbonate, organic matter, and Fe–Mn oxyhydroxide phases (e.g. Freydier et al., 2001; Gourlan et al., 2008, 2010; Le Houedec et al., 2012, 2016). The leaching and analyses were mostly conducted at CEREGE following

**Table 3**
Neodymium isotope composition of bulk sediment leachates from the Mediterranean Sea over the S1-equivalent period.

| Sample depth (cm)[a] | Age[b] | $\varepsilon_{Nd}$ ± 2SD | Carbonate[c] | Source[d] |
|---|---|---|---|---|
| **BC07** (33°40.0′N, 32°40.0′E; 893 m) | | | | |
| 0.25 | 0.8 | −4.6 ± 0.2 | 73% | 1 |
| 5.25 | 2.6 | −6.2 ± 0.2 | 69% | 1 |
| 10.25 | 4.4 | −5.5 ± 0.2 | 54% | 1 |
| 15.25 | 6.1 | −4.8 ± 0.2 | 64% | 1 |
| 20.25 | 7.9 | −5.8 ± 0.2 | 61% | 1 |
| 22.25 | 8.6 | −5.9 ± 0.2 | 61% | 1 |
| 24.25 | 9.3 | −5.9 ± 0.2 | 52% | 1 |
| 26.25 | 10.0 | −4.4 ± 0.2 | 54% | 1 |
| 29.75 | 11.2 | −5.0 ± 0.2 | 56% | 1 |
| 31.75 | 12.0 | −4.7 ± 0.2 | 54% | 1 |
| 36.25 | 13.5 | −4.2 ± 0.2 | 58% | 1 |
| 40.25 | 14.9 | −4.6 ± 0.2 | 67% | 1 |
| 48.25 | 17.8 | −4.3 ± 0.2 | 66% | 1 |
| **BC19** (33°47.9′N, 28°36.5′E; 2750 m) | | | | |
| 0.25 (1 M HCl) | 0.9 | −6.3 ± 0.2 | 68% | 2 |
| 0.25 (HH) | | −5.5 ± 0.2 | n.d. | 2 |
| 3.75 (1 M HCl) | 2.0 | −7.3 ± 0.2 | 69% | 2 |
| 3.75 (1 M acetic acid) | | −7.5 ± 0.2 | 69% | 2 |
| 3.75 (25% acetic acid) | | −7.6 ± 0.2 | 68% | 2 |
| 5.75 | 2.8 | −7.5 ± 0.2 | 64% | 1 |
| 7.25[e] | 3.4 | −5.2 ± 0.2 | 67% | 1 |
| 12.75 | 5.1 | −7.8 ± 0.2 | 70% | 1 |
| 15.75 | 6.1 | −5.0 ± 0.2 | 66% | 1 |
| 19.25 | 7.1 | −5.0 ± 0.2 | 70% | 1 |
| 20.75[f] | 7.6 | −5.4 ± 0.2 | 51% | 1 |
| 23.25 | 8.3 | −4.1 ± 0.2 | 58% | 1 |
| 25.75[f] | 9.1 | −4.1 ± 0.2 | 53% | 1 |
| 27.25 | 9.6 | −4.5 ± 0.2 | 55% | 1 |
| 29.25 | 10.1 | −4.3 ± 0.2 | 50% | 1 |
| 30.25 | 10.4 | −4.3 ± 0.2 | 52% | 1 |
| 32.25[f] | 11.1 | −4.8 ± 0.2 | 49% | 1 |
| 34.95 | 12.0 | −5.5 ± 0.2 | 62% | 1 |
| **ABC26** (33°21.3′N, 24°55.7′E; 2150 m)[g] | | | | |
| 1.0 (BC03; 1 M HCl) | ∼1 | −7.1 ± 0.2 | 75% | 2 |
| 1.0 (BC03; HH) | ∼1 | −6.4 ± 0.2 | n.d. | 2 |
| 5.6 (ABC26; 1 M HCl) | 2.7 | −7.2 ± 0.2 | 62% | 2 |
| 12.5 (SL125; 1 M HCl) | ∼6 | −5.7 ± 0.2 | 66% | 2 |
| 12.5 (SL125; HH) | ∼6 | −3.6 ± 0.2 | n.d. | 2 |
| **SL114** (35°17.2′N, 21°24.5′E; 3390 m) | | | | |
| 0.25 | 0.1 | −7.8 ± 0.2 | 72% | 2 |
| 15.55 | 4.0 | −7.0 ± 0.2 | 61% | 3 |
| 24.05 | 6.8 | −5.0 ± 0.2 | 68% | 3 |
| 28.05 | 8.1 | −5.8 ± 0.2 | 58% | 3 |
| 32.05 | 9.4 | −5.0 ± 0.2 | 63% | 3 |
| 34.05 | 10.1 | −6.4 ± 0.2 | 62% | 3 |
| 39.05 | 11.7 | −6.9 ± 0.2 | 56% | 3 |
| 49.20 | 15.0 | −8.2 ± 0.2 | 52% | 3 |
| **MT15** (38°53.8′N, 04°30.6′E, WMS; 2373 m) | | | | |
| 0.25 (1 M HCl) | 0.9 | −9.3 ± 0.2 | 55% | 2 |
| 0.25 (25% acetic acid) | | −9.3 ± 0.2 | 56% | 2 |
| 0.25 (HH) | | −9.2 ± 0.2 | n.d. | 2 |
| 20.25 | 3.1 | −8.8 ± 0.2 | 67% | 3 |
| 50.25 | 6.4 | −9.3 ± 0.2 | 60% | 3 |
| 80.25 | 9.6 | −9.2 ± 0.2 | 58% | 3 |
| 90.25 | 10.7 | −9.1 ± 0.2 | 57% | 3 |
| 100.25 | 11.8 | −9.5 ± 0.2 | 47% | 3 |
| 108.00 | 12.7 | −9.8 ± 0.2 | 48% | 3 |
| 114.00 | 13.3 | −8.9 ± 0.2 | 51% | 3 |
| 118.00 | 13.8 | −9.6 ± 0.2 | 54% | 3 |
| 120.25 | 14.0 | −9.1 ± 0.2 | 58% | 3 |
| 140.00 | 16.1 | −9.3 ± 0.2 | 49% | 3 |

[a] Selected samples were done with different leaching agents. Note that HH (i.e. hydroxylamine hydrochloride) was performed on decarbonated samples.
[b] Ages (in cal. kyr BP) are newly provided in this contribution (see Supplementary information).
[c] Weight loss after leaching is calculated to approximately represent carbonate content; n.d. = not determined.
[d] 1 = Freydier et al. (2001), 2 = Tachikawa et al. (2004), 3 = this study.
[e] The sample is likely affected by Santorini tephra, and thus not shown in Fig. 4.
[f] For these samples, normalized REE patterns are presented to confirm the seawater origin of leachate $\varepsilon_{Nd}$ signals (see Supplementary information).
[g] Data of nearby cores BC03 (33°22.5′N, 24°46.0′E; 2180 m) and SL125 (33°39.4′N, 24°33.0′E; 1946 m) are reported.

the analytical procedures described previously, having an overall 2SD data uncertainty of 0.3 $\varepsilon_{Nd}$-unit (Freydier et al., 2001; Tachikawa et al., 2004). For evaluating the leaching performance, weight loss after leaching was calculated to represent carbonate content, of which the validity was confirmed by direct carbonate determinations done at Utrecht (Table 3). Different leaching agents such as 1 M HCl, 1 M and 25% acetic acid, and hydroxylamine hydrochloride (HH) of decarbonated samples were tested and the results have been reported (Tachikawa et al., 2004), and re-evaluated with other data here (Table 3).

The $\varepsilon_{Nd}$ data for cores BC07 and BC19 and for the core-top samples of SL114 and MT15 have been published (Freydier et al., 2001; Tachikawa et al., 2004), whereas all other SL114 and MT15 data are reported here (Table 3).

## 3. Results

An overview and information on investigated cores is given (Table 1; Fig. 1). Our results (Tables 2 and 3) are plotted against water-depth in Fig. 2, along longitude in Fig. 3, and versus time in Fig. 4.

Overall, the $\varepsilon_{Nd}$ values from all EMS cores below 800 m water-depth are characterized by very homogeneous bottom-water signatures for the S1-period: −5.3 to −4.5 ± 0.3 (Fig. 2). In addition, these $\varepsilon_{Nd}$ data show a small but systematic increase from west to east (Fig. 3). By contrast, the sample from core BP15, located at a water-depth of 665 m, has a much less radiogenic value (−6.1 ± 0.5) (Figs. 2 and 3). The somewhat larger error of BP15 sample is because of the small amount of Nd that was analyzed (Table 2). Notably, the foraminiferal and fish samples from cores SL139 and GC21, respectively, which have nearly identical location and water-depth, give the same $\varepsilon_{Nd}$ values (Tables 1 and 2). This supports the validity of bottom-water $\varepsilon_{Nd}$ signatures from planktonic foraminifera herein.

During the whole S1-period, the $\varepsilon_{Nd}$ (fish debris) of core CP10 varies within the analytical uncertainty (−5.3 to −4.7 ± 0.3) (Fig. 4). Yet, these values seem to be slightly more radiogenic in the S1a than S1b intervals. At the end of sapropel S1 formation (∼6.1 kyr BP), CP10 reports the lowest $\varepsilon_{Nd}$ value of −5.3 ± 0.3. Similarly, the ABC26 fish-debris derived record may have a decline within S1-period; and this is especially obvious when considering the leachate $\varepsilon_{Nd}$ data-point at S1 termination from nearby core SL125 (Tachikawa et al., 2004; Tables 2 and 3) (Fig. 4).

This S1a–S1b difference is also observed in the leachate data of core BC19 (Freydier et al., 2001; Tachikawa et al., 2004; Tables 2 and 3). Therefore, although this trend is within error for each core, it appears to be systematic for all EMS cores (Fig. 4). Note that some S1b samples were taken from the post-depositionally oxidized section; this is unlikely to affect the $\varepsilon_{Nd}$ signature preserved in fish debris/teeth (Martin and Scher, 2004) (Table 2), and neither for those recorded in our leachates as revealed by the negative Ce anomaly (see Supplementary information).

Furthermore, cores SL114, ABC26, and BC19 show distinct differences between S1 and non-S1 sediments (Freydier et al., 2001; Tachikawa et al., 2004; Tables 2 and 3). The leachate $\varepsilon_{Nd}$ values are more radiogenic during S1-period (−5.8 to −4.1) than during the intervals before and after (−8.2 to −5.5) (Fig. 4). By contrast, core BC07 located at the easternmost Levantine, displays a generally de-

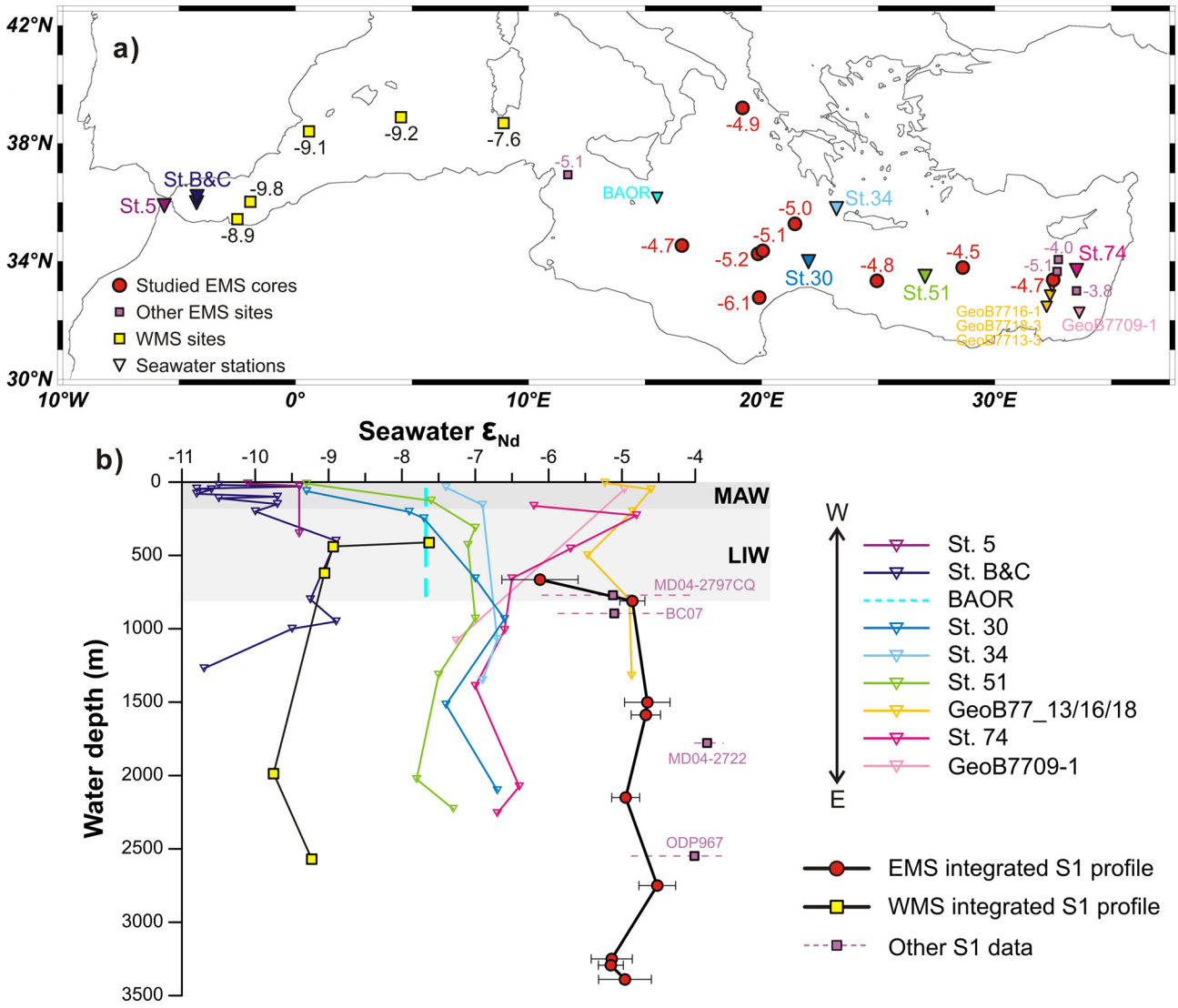


**Fig. 2.** Paleo-seawater $\varepsilon_{Nd}$ signatures for the sapropel S1 time, compared to modern *in-situ* seawater data. (a) Average $\varepsilon_{Nd}$ values for the S1-period, from the EMS (red-circles: Table 2; purple-squares: Freydier et al., 2001; Scrivner et al., 2004; Cornuault et al., 2018), and WMS (yellow-squares: Jiménez-Espejo et al., 2015; Dubois-Dauphin et al., 2017; Table 3). Note that sapropel S1 is absent in the WMS, thus the data refer to a S1-equivalent age. For the archives of paleo-seawater $\varepsilon_{Nd}$ data see the legend of Fig. 4. The colored triangles indicate seawater stations, corresponding to the colored vertical profiles in (b). (b) Average seawater-$\varepsilon_{Nd}$ values of the S1-period versus water-depth for the integrated EMS (red-circles), compared to the modern seawater depth-profiles (Henry et al., 1994; Tachikawa et al., 2004; Vance et al., 2004). The integrated WMS profile (yellow-squares) and other published S1 data (purple-squares) are also shown. Note that nearby stations are combined to give representative depth-profiles for the Nile deep-sea fan (GeoB77_13/16/18; Vance et al., 2004) and for the waters across the Strait of Gibraltar (St. B&C; Tachikawa et al., 2004). The BAOR was combined from seawater samples of 100, 200, 400, and 800 m depths, monitoring the westward-flowing LIW through the Strait of Sicily (Henry et al., 1994).

creasing trend over the past 18 kyr (leachate $\varepsilon_{Nd}$: −6.2 to −4.2) (Freydier et al., 2001; Tachikawa et al., 2004) (Table 3; Fig. 4). For the WMS, core MT15 shows relatively invariant changes with no discernible pattern throughout the Holocene (leachate $\varepsilon_{Nd}$: −9.6 to −8.8) (Freydier et al., 2001; Tachikawa et al., 2004; Table 3) (Fig. 4).

Notably, Table 3 summarizes both new and published $\varepsilon_{Nd}$ data (Freydier et al., 2001; Tachikawa et al., 2004), with ages newly given. Detailed data sources refer to Table 3. The EMS $\varepsilon_{Nd}$ modeling results are shown in Fig. 5, with parameters motivated in Supplementary information.

## 4. Discussion

### 4.1. Diagnostic sources of Nd for the Mediterranean Sea

Available seawater data for the recent Mediterranean (Fig. 1b) suggest that the dissolved Nd concentration and $\varepsilon_{Nd}$ composition of the west-to-east flowing waters through the straits of Gibraltar and of Sicily are lower and less radiogenic than those flowing east-to-west (Spivack and Wasserburg, 1988; Henry et al., 1994; Tachikawa et al., 2004). A substantial source of radiogenic Nd is thus required to explain this basin-wide imbalance in Nd concentration and isotope distribution. Firstly, the generally higher dissolved Nd concentration of surface-compared to deep-waters indicates that this source may be related to partial dissolution of aeolian or riverine particles; secondly, the west–east gradients in dissolved Nd- and $\varepsilon_{Nd}$-values suggest a radiogenic end-member source in the east (Frost et al., 1986; Spivack and Wasserburg, 1988; Henry et al., 1994; Tachikawa et al., 2004; Vance et al., 2004; Ayache et al., 2016).

Saharan dust is the dominant detrital component of recent Mediterranean sediments. However, considering its rather unradiogenic $\varepsilon_{Nd}$ signatures (∼−13 to −10; Frost et al., 1986; Scheuvens et al., 2013), its relatively low Nd content and low fractional solubility, an aeolian Nd contribution is considered insignificant

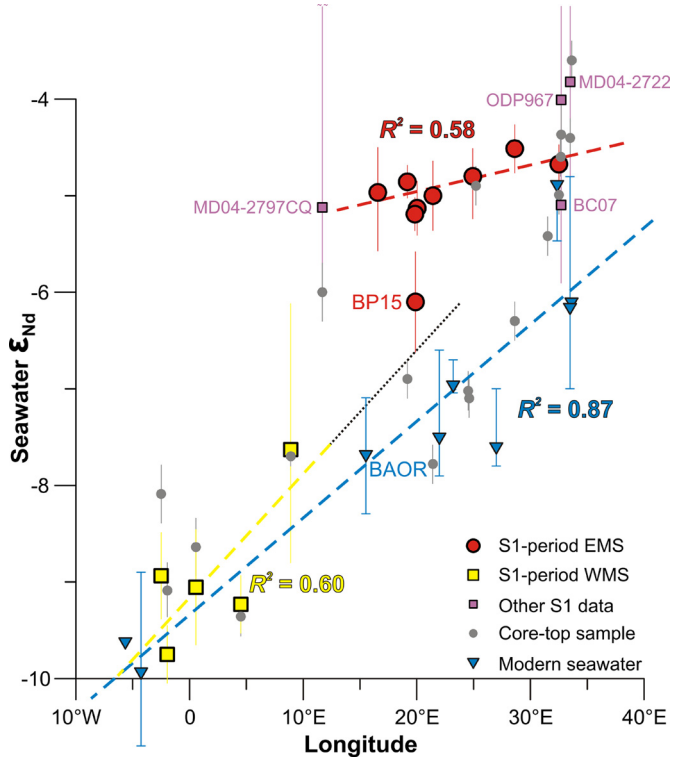


**Fig. 3.** Average seawater-$\varepsilon_{Nd}$ values versus longitude for the sapropel S1 time and for the present-day. The S1-period data are distinguished between EMS (red circles: this study; Table 2), WMS (yellow squares: Jiménez-Espejo et al., 2015; Dubois-Dauphin et al., 2017; Table 3), and other S1 data (purple squares: Freydier et al., 2001; Scrivner et al., 2004; Cornuault et al., 2018). Core-top samples represent the recent bottom-water $\varepsilon_{Nd}$ signatures (grey circles: Freydier et al., 2001; Scrivner et al., 2004; Tachikawa et al., 2004; Jiménez-Espejo et al., 2015; Dubois-Dauphin et al., 2017; Cornuault et al., 2018; Tables 2 and 3). The data ranges and/or 2SD errors are shown. Note that red regression-line is for our S1-period EMS data alone (i.e. excluding other S1 data). Yellow regression-line and its prolonged black stippled-line indicate the link between WMS and the shallow EMS core BP15 during S1-period. Blue triangles and trend-line indicate a progressive west–east increase in dissolved $\varepsilon_{Nd}$ of modern seawater; blue error-bars depict the $\varepsilon_{Nd}$ ranges of >200 m water-column (Henry et al., 1994; Tachikawa et al., 2004; Vance et al., 2004).

(Tachikawa et al., 2004; Ayache et al., 2016). This must especially be true for the humid sapropel intervals, characterized by largely decreased dust fluxes (Wu et al., 2017; also see Supplementary information).

By contrast, the Nile is the only known source that could deliver accountable amounts of radiogenic Nd to the Mediterranean. At present, the most-radiogenic dissolved $\varepsilon_{Nd}$ values (−4.8 to −4.5) were found at >200 m water-depth in the easternmost Levantine (Tachikawa et al., 2004; Vance et al., 2004), thought to relate to Nile-derived material (Freydier et al., 2001; Scrivner et al., 2004). The partially dissolved Nile particles, rather than the river water itself, were reported to provide large amounts of radiogenic Nd to the EMS; however, the EMS dissolved $\varepsilon_{Nd}$ value calculated from estimated Nile-related fluxes was less radiogenic than the observed data for the modern EMS (Tachikawa et al., 2004). The missing radiogenic source could be either from changes in dissolved–particulate interaction on the Nile deep-sea fan, or on other margins that are characterized by relatively radiogenic $\varepsilon_{Nd}$ ranges, such as Aegean and western Ionian (Ayache et al., 2016). The high-resolution modeling including all potential margin-interactions, however, obtained too radiogenic values not only for deep- but for all modern Mediterranean waters (Ayache et al., 2016). As the combined observations of Nd concentration and isotope composition rather point to a dominant shallow, eastern source, this can only relate to the Nile (Fig. 1b).

Indeed, the west–east increasing trends in dissolved Nd- and $\varepsilon_{Nd}$-values for both present-day and S1-period indicate a two-end-member mixing between the radiogenic Nile runoff in the east, and the less radiogenic Atlantic waters inflow from the west (Figs. 1 and 3). This is also corroborated by our modeling results of the Nd budget, exhibiting a present-day EMS situation consistent with the modern seawater data (Fig. 5a). Therefore, to the first order, seawater-$\varepsilon_{Nd}$ changes can be interpreted as changes in the Nile contribution relative to the Atlantic-derived contribution to the EMS.

### 4.2. EMS seawater $\varepsilon_{Nd}$ as related to S1 deep-water stagnation

The $\varepsilon_{Nd}$ values from all EMS cores below ~800 m water-depth are very radiogenic and homogeneous (−5.3 to −4.5 ± 0.3) during the S1-period, indicating a uniform bottom-water signature during that time (Table 2; Fig. 2). This is in contrast to the much less radiogenic and more heterogeneous $\varepsilon_{Nd}$ values reported for the modern EMS deep waters (−7.8 to −6.4 for basin-wide >800 m depth, except about −5 for the Nile deep-sea fan; Tachikawa et al., 2004; Vance et al., 2004) (Fig. 2b). The differences in seawater-$\varepsilon_{Nd}$ values and in associated west–east gradients between present-day and S1-period indicate that the ratios for the fluxes of more radiogenic Nile-derived Nd relative to less radiogenic Atlantic-origin Nd were augmented during the S1-period (Figs. 2 and 3). Moreover, the spatially and temporally constant $\varepsilon_{Nd}$ values correspond to a longer residence time for the deep-water masses (Tables 2 and 3; Figs. 2–4). These results are in good agreement with the sluggish circulation, reduced ventilation, and stagnant, anoxic deep-water conditions, as reported for the EMS during S1 formation (e.g. Rossignol-Strick, 1983; Rohling, 1994; Emeis et al., 2000; De Lange et al., 2008).

The S1 sample from core BP15, located at a water-depth of 665 m, has an intermediate $\varepsilon_{Nd}$ value (−6.1 ± 0.5) (Table 2; Fig. 2). This may reflect paleodrainage runoff from the wider North-African margin during the S1-period (Figs. 1 and 2). In sapropel times, precession-forced intensified monsoon precipitation could have reactivated fossil river/wadi systems over the Libyan–Tunisian regions (Scrivner et al., 2004; Osborne et al., 2010; Wu et al., 2016, 2017). However, such enhanced runoff and sediment transport should also have had a prominent impact on the $\varepsilon_{Nd}$ at site CP10 (1501 m depth), which was not observed (Wu et al., 2016). Thus, although this effect cannot be fully excluded, it is unlikely to be a major factor.

Alternatively, combined with the basin-wide homogeneous deep-water $\varepsilon_{Nd}$ signature, the deviating $\varepsilon_{Nd}$ value of BP15 may indicate a boundary in the EMS, between more stagnant waters below and waters with more frequent renewal above ~800 m depth. This interpretation is consistent with various proxy and simulation reconstructions for the S1-period. Reduced, depth-dependent ventilation conditions were shown for a water column of ~700–2300 m depth for the eastern Levantine (Tachikawa et al., 2015). Benthic foraminiferal investigations have also revealed a basin-wide shallowing of vertical convection during the S1 phase, but superimposed by local signals (Schmiedl et al., 2010).

In fact, the S1 dysoxic/anoxic conditions could have existed at shallower depths on the Nile deep-sea fan, as revealed by the intense anaerobic microbial activity at 1155 m depth seafloor (Bayon et al., 2013). This is corroborated by redox-proxy studies, showing that persistent S1-anoxia may reach depths as shallow as ~900 m in this area (Matthews et al., 2017), and the fluctuating redox states during S1 as inferred from a 550 m-depth, Nile-fan record (Hennekam et al., 2014). These observations may be shallower than the reported anoxic boundary at ~1800 m depth throughout the EMS (De Lange et al., 2008), due to enhanced Nile runoff and nutrient inputs. This not only caused a

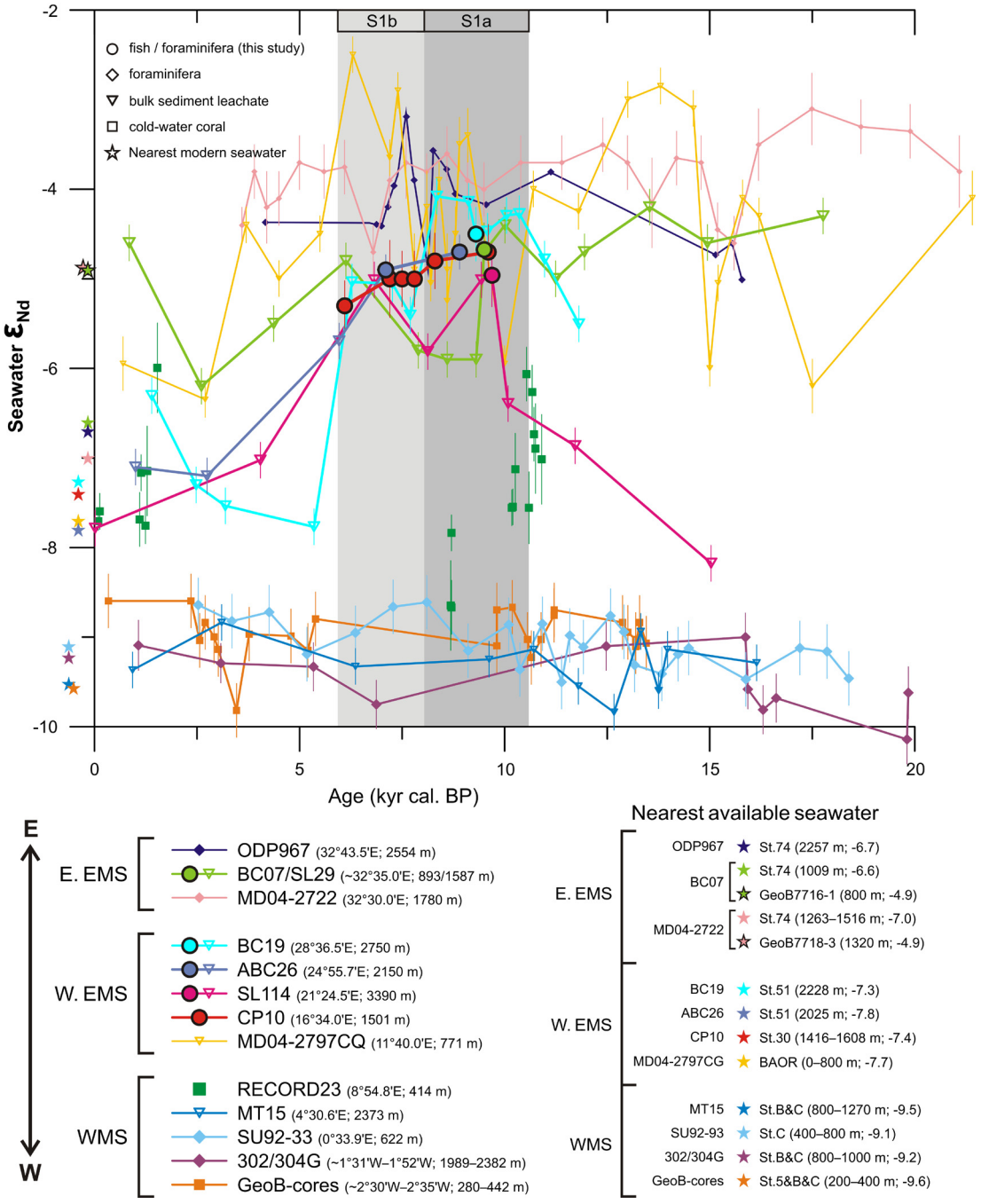


**Fig. 4.** Reconstructed seawater-$\varepsilon_{Nd}$ changes in the studied cores (CP10, ABC26, SL114, BC19, and MT15; Tables 2 and 3; Fig. 1) over the S1-equivalent period, in comparison with existing records in the Mediterranean Sea (Freydier et al., 2001; Scrivner et al., 2004; Tachikawa et al., 2004; Jiménez-Espejo et al., 2015; Dubois-Dauphin et al., 2017; Cornuault et al., 2018). The data from different archives are distinguished by different symbols, and 2SD error bars are shown. Note that the ABC26 record is composed of data from three nearby cores (ABC26, BC03, SL125; Table 3). Longitude and water-depth of the records are indicated in legend. Nearest seawater $\varepsilon_{Nd}$ data, are taken from an approximate depth at the closest available location to the cores/sites (Henry et al., 1994; Tachikawa et al., 2004; Vance et al., 2004).

locally more stratified water column but also high organic-matter fluxes and related high oxygen-consumption rates, i.e. oxygen-depleted conditions (Stratford et al., 2000; Bianchi et al., 2006; Schmiedl et al., 2010).

Taking all together, we argue for a deep-water stagnation below ~800 m depth over the EMS during most of the S1-period. This was likely accompanied by local and/or regional differences in water-column ventilation, which for coastal areas with enhanced river runoff (e.g. Nile) may have been shallower than elsewhere. We further propose that the $\varepsilon_{Nd}$ signal could be related to the degree of EMS deep-water stagnation, to a certain extent. This is based on the assumption that the intensity of the Nile runoff predominantly delivering radiogenic Nd into the EMS is directly related to the strength of the deep-water stagnation during sapropels, as supported by paleoceanographic modeling (Myers et al., 1998; Myers, 2002).

### 4.3. Variability of EMS stagnation and circulation over the S1-period

Despite the complexity in extracting seawater-$\varepsilon_{Nd}$ signals from different archives via various approaches, the reliability of our data, in particular for those from bulk sediment leachates has been explicitly verified. Several lines of evidence are provided from two

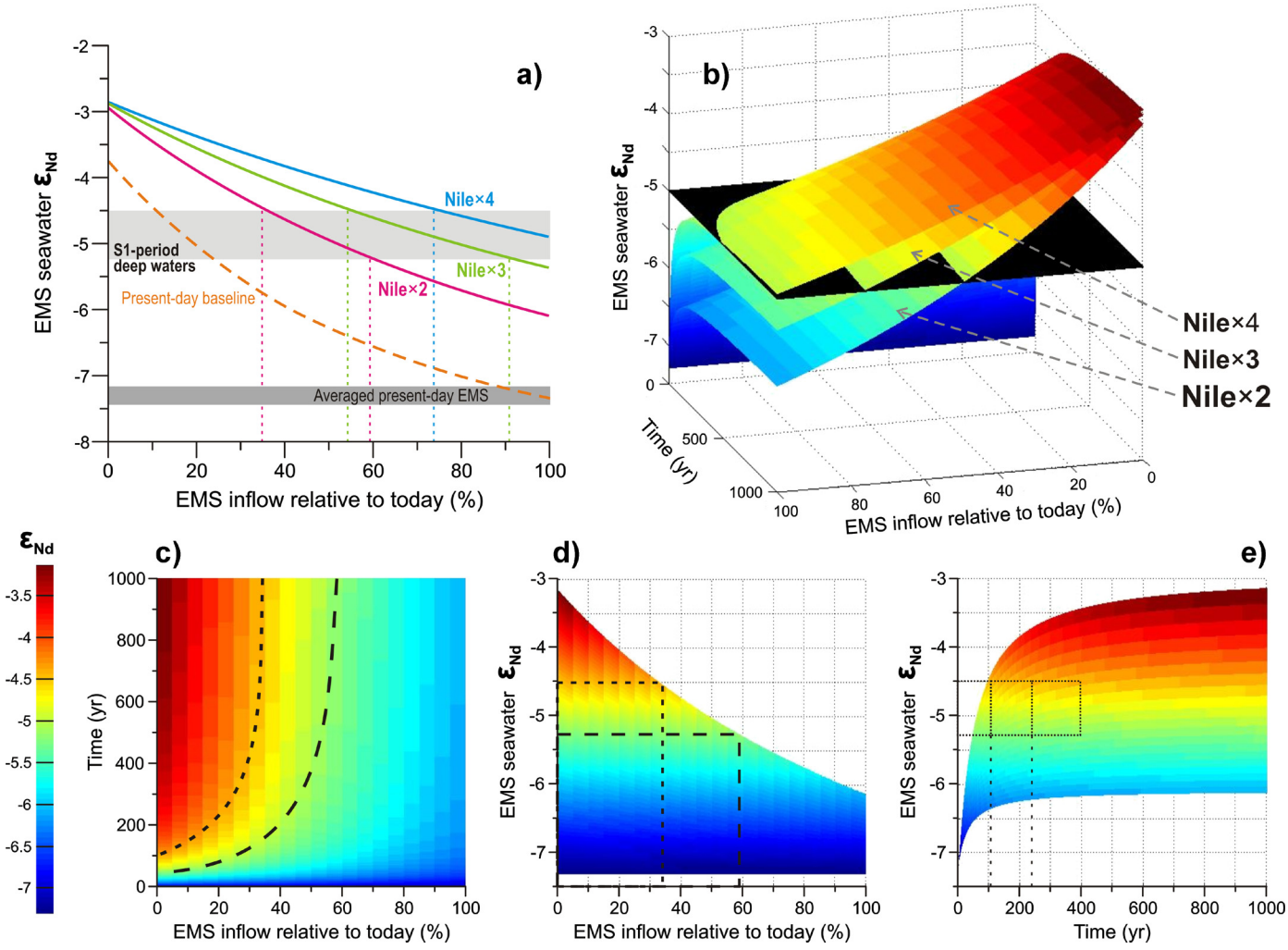


**Fig. 5.** Modeling results of Nd in the EMS for sapropel S1 formation. (a) Sensitivity tests of the EMS seawater-$\varepsilon_{Nd}$ as a function of Nd fluxes from the WMS (EMS inflow, i.e. MAW) and from the Nile River during pre-S1/S1 time (for details see Supplementary information). With the present-day EMS baseline yielded (i.e. Nile×1, Dust×1) that is well consistent with the seawater-$\varepsilon_{Nd}$ data (Tachikawa et al., 2004), three S1-scenarios with different Nile discharges are tested: ×2, ×3, ×4 (Grimm et al., 2015), along with a constant Saharan dust flux (25% of today; Wu et al., 2017) over the S1-period. (b) The 3D plot of three S1-scenarios with different Nile discharges, showing a black-surface of averaged S1-seawater $\varepsilon_{Nd}$ (−5.3 to −4.5 ± 0.3; Table 2). A modeled time of 1000 yr is shown. The most realistic scenario of Nile×2 is elaborated from different perspectives in the following plots: (c) Time vs. EMS inflow, (d) EMS seawater-$\varepsilon_{Nd}$ vs. EMS inflow, and (e) EMS seawater-$\varepsilon_{Nd}$ vs. time.

aspects. Firstly, data comparison has been thoroughly performed, such as comparing data between different archives, different leaching methods, and between our leachate-$\varepsilon_{Nd}$ values of core-top sediments and data of modern *in-situ* seawater. Secondly, results for a variety of analyses are presented to evaluate the leaching performance, thereby confirming the applicability of seawater-derived Nd extraction for the Mediterranean carbonate-rich sediments. This includes bulk carbonate contents, as well as Nd isotopes, Nd concentrations, and REE patterns of both the leachate and residue fractions. The evidence and detailed arguments are presented in Supplementary information, which allows changes in the deep-water stagnation and EMS circulation across the S1-period to be reconstructed.

Based on fish debris/teeth, the bottom-water $\varepsilon_{Nd}$ record of core CP10 (−5.3 to −4.7 ± 0.3) indicates that the EMS stagnation may have persisted throughout the S1-period (Table 2; Fig. 4). The $\varepsilon_{Nd}$ values seem to be more radiogenic in the S1a than S1b, and decrease towards the end of S1 formation (Fig. 4). Although this trend is within the analytical uncertainties, it is systematically shown in archived $\varepsilon_{Nd}$ records of cores BC19 and ABC26/BC03 (Freydier et al., 2001; Tachikawa et al., 2004; Tables 2 and 3) (Fig. 4). In other words, these consistent differences may indicate a higher degree of EMS deep-water stagnation, and thus a more limited exchange with the WMS during S1a than S1b. This is supported by various micropalaeontological and geochemical studies, indicating more frequent ventilation pulses in EMS areas at 500–2300 m depth after 8.2 kyr BP (e.g. Kuhnt et al., 2008; Schmiedl et al., 2010; Revel et al., 2015; Tachikawa et al., 2015; Matthews et al., 2017; Tesi et al., 2017), and even more so after 7.5 kyr BP (Filippidi et al., 2016). Although the S1a–S1b difference is not clearly observed for deep-water site SL114 (Fig. 4), it has been reported for a 3400 m-depth EMS core in terms of the mean frequency of variable ventilation rate (Jilbert et al., 2010).

The BC19, ABC26, and SL114 $\varepsilon_{Nd}$ records display distinct differences between S1 and non-S1 sediments (Fig. 4). Before and after the S1-period the much less radiogenic values reflect efficient deep-water ventilation in the EMS. By contrast, the more radiogenic $\varepsilon_{Nd}$ during and immediately prior to the S1-period point to intensified Nile runoff and reduced EMS circulation that may have initiated thousand(s) of years before S1 formation started (Fig. 4). This observation not only coincides with the onset of Nile flooding ~2–5 kyr prior to the S1 onset (Hennekam et al., 2014, 2015; Revel et al., 2015; Tachikawa et al., 2015), but also with a 3-kyr precession lag of sapropels, related to the occurrence of North Atlantic cold events (Ziegler et al., 2010).

This pre-S1 conditioning observed in our $\varepsilon_{Nd}$ records, is also consistent with reported oxygen-depleted conditions for bottom waters (500–2300 m depth) starting around 16–11 kyr BP in the Nile and Adriatic areas (Schmiedl et al., 2010; Grimm et al., 2015; Tachikawa et al., 2015; Tesi et al., 2017). During the preconditioning period, the circulation and deep-water formation were continuously weakening but still active, allowing the radiogenic $\varepsilon_{Nd}$ signature of the enhanced Nile fluxes to be transferred to the deep water. Accordingly, the Nile-derived $\varepsilon_{Nd}$ imprinted the water column from deep to shallow before the S1 onset. Due to the stagnating conditions, this signal remained in the deep water, only to be altered by re-ventilation events.

The synchronous S1 onset across the entire EMS suggests a basin-wide triggering mechanism – a weakening of the LIW which hampered dense water formation (De Lange et al., 2008; Schmiedl et al., 2010; Tesi et al., 2017). Subsequently, the deep-water stagnation maintained over the whole S1-period, and ended synchronously with the S1 termination (Fig. 4). This abrupt renewal of deep waters at the S1 ending, as observed in BC19, ABC26/SL125, and SL114, is in line with the simultaneous recovery of benthic ecosystems in >1800 m-depth areas (De Lange et al., 2008; Schmiedl et al., 2010; Tachikawa et al., 2015).

By contrast, for the cores close to the Nile deep-sea fan, no discernable differences between the pre-S1, S1, and post-S1 intervals are observed (Fig. 4). The cores include BC07 (Freydier et al., 2001), ODP967 (Scrivner et al., 2004), and MD04-2722 (Cornuault et al., 2018), although their seawater-$\varepsilon_{Nd}$ records were derived from different archives and methods. This can be attributed to a direct and persistent control of the Nile discharge on the easternmost Levantine, as confirmed by the small $\varepsilon_{Nd}$ differences between the S1 data, core-top samples, and modern seawater for the areas east of ~30°E, which are all characterized by spatially variable $\varepsilon_{Nd}$ signatures (Fig. 3). Being spatially specified, the large $\varepsilon_{Nd}$ range for this small area may further reflect the variable influence of surface-water currents (Hennekam et al., 2015).

The average, S1-aged $\varepsilon_{Nd}$ values for core MD04-2797CQ in the Strait of Sicily are in agreement with our basin-wide EMS signature (Figs. 2 and 3). However, the core-top value is more radiogenic than that of the corresponding modern seawater, as reported in previous studies (Henry et al., 1994; Tachikawa et al., 2004) and in Cornuault et al. (2018) (Figs. 3 and 4). One possible explanation is that some EMDW was entrained with the outflowing LIW and is recorded in the deepest parts of the Strait of Sicily (771 m depth). This is likely because of the shallower S1 boundary of intermediate/deep waters, despite a weaker LIW, as discussed above. If so, this suggests minor exchange of deep waters to the WMS during the S1-period (also see Section 4.5). Further investigations are needed to substantiate this hypothesis.

### 4.4. EMS-$\varepsilon_{Nd}$ modeling of Nile versus Atlantic contributions

Based on the balances in terms of water mass, Nd, and Nd isotopes, we set up a box model (after Tachikawa et al., 2004) to investigate the first-order variability of the Nd budget, as related to riverine supplies to the EMS (i.e. Nile forcing) and water exchange between the EMS and WMS (i.e. circulation effect). Either or both of these changes are required to obtain the more radiogenic and homogeneous deep-water $\varepsilon_{Nd}$ signatures (−5.3 to −4.5 ± 0.3; Table 2) during the S1-period compared to the present, as found in this study. Specifically, along with partially dissolved Saharan dust fluxes that were largely reduced during the S1-period, a radiogenic Nile input, and an unradiogenic Atlantic-derived WMS input are considered major Nd sources to the EMS.

All modeling experiments are initialized with the Nd budget and general settings which resemble the present-day EMS. This practice, the same as done in various EMS modeling studies (e.g. Myers et al., 1998; Stratford et al., 2000; Bianchi et al., 2006; Grimm et al., 2015; Cornuault et al., 2018), is supported by our data, especially those from sediment-leachates of the EMS deep-water sites (i.e. BC19, SL114, and ABC26/BC03/SL125). These $\varepsilon_{Nd}$ values are not only similar for the pre-S1 and post-S1 intervals, but are also distinctly different between non-S1 and S1 periods (Table 3; Fig. 4).

A present-day baseline fully consistent with the EMS *in-situ* seawater data (Tachikawa et al., 2004) is simulated, justifying the parameters used in the model (Fig. 5a). For the S1-period, three scenarios with different Nile discharges are tested: ×2, ×3, ×4 (Grimm et al., 2015), accompanied by a constant Saharan dust flux (25% of today; Wu et al., 2017). Coherent with other studies, a 2% partial Nd dissolution is used for Saharan dust (Tachikawa et al., 2004) and Nile particles (Cornuault et al., 2018). Validity of the modeling settings and scenarios is motivated in detail in Supplementary information.

The modeling (Fig. 5) shows that with a 2-fold (or 3-fold) increased Nile discharge, a 40–65% (or 10–45%) reduction of inflowing MAW is needed to account for the observed seawater-$\varepsilon_{Nd}$ in a basin-wide EMS during the S1-period. These results are consistent with a reduced but continued MAW inflow, as revealed by the weaker but still existing west–east gradients in seawater-$\varepsilon_{Nd}$ data (Table 2; Fig. 3) and in planktonic foraminiferal $\delta^{18}O$ (Rohling and De Rijk, 1999; Emeis et al., 2000) for S1 than today. For the anticipated most-extreme scenario – a 4-fold increased Nile input – this would still correspond to an average 10% (0–25%) reduction of the EMS inflow. Indeed, recent ocean-biogeochemical modeling study has also suggested that enhanced freshwater and nutrient inputs from the Nile alone cannot explain the deep-water anoxic conditions necessary for S1 formation (Grimm et al., 2015).

The Nd input of Nile×2 is considered to be the most-realistic scenario, rather than that of Nile×3, which is mainly because the potential maximum values for dissolved Nd fluxes from the Nile are used in the modeling (see Supplementary information). Firstly, the pre-Aswan Nile, including sediment- and water-fluxes, is used as the baseline (Grimm et al., 2015). Secondly, a relatively high dissolution rate (2%) is used, causing a predominantly particle dissolved Nd (~90%) for the total Nile-related Nd fluxes (Cornuault et al., 2018). Thirdly, the upper limit of the Nile water dissolved Nd concentration (100–400 pmol/kg; Scrivner et al., 2004) is taken. Most importantly, for S1 scenarios, the sediment-related flux is assumed to be proportional to the Nile water flux. This is probably not the case, as the S1 sediment flux may have been similar as today due to the monsoon-generated denser vegetation cover on the Nile-particle source areas (Hennekam et al., 2014, 2015). In addition, the offshore Nile-sediment spreading must be limited to within the eastern Levantine, being mostly deposited on the Nile delta (Hennekam et al., 2015; Wu et al., 2016, 2017). This may have resulted in the small differences in $\varepsilon_{Nd}$ values between the S1-period and the present-day (and other non-S1 intervals) for the area east of 30°E (Figs. 3 and 4).

Assuming the Nd oceanic cycle to be fully conservative, the Nile×2 scenario gives a residence time for the EMS seawater of ~140 ± 40 yr during the S1-period, compared to the estimates of 45 ± 15 yr for the present (Tachikawa et al., 2004; Rohling et al., 2015) (Fig. 5c–e). For modeling-related details see Supplementary information.

### 4.5. EMS–WMS exchange with implications for circulation dynamics

To sum up, our results and associated interpretations give a representative and fully consistent picture of the EMS dynamics and composition, in view of the following: 1) our study has basin-wide core/sample coverage in the EMS (Table 1; Fig. 1); 2) our data are mainly based on fish debris/teeth recognized as the most-reliable

bottom-water $\varepsilon_{Nd}$ archive, supplemented with foraminiferal tests and bulk sediment leachates (Tables 2 and 3); 3) the various archives used, give mutually consistent $\varepsilon_{Nd}$ values and have proven to faithfully record the paleo-seawater composition (Figs. 2–4); and 4) the differences between non-S1 and S1 samples, and the west–east gradient observed in our seawater-$\varepsilon_{Nd}$ data are paleoceanographically consistent (Figs. 3 and 4), and are quantitatively supported by modeling results (Fig. 5).

At present, deep waters in the EMS and WMS seem largely coupled, as observed from a rather continuous gradient in modern seawater-$\varepsilon_{Nd}$ across both basins (Figs. 2 and 3). By contrast, the deep waters for EMS and WMS appear mostly decoupled during the S1-equivalent period (but a minor exchange may have existed; see Section 4.3). The WMS, compared to the EMS, has a more heterogeneous water column and a stronger west–east gradient with respect to the $\varepsilon_{Nd}$ signature (Figs. 2 and 3). Consequently, the S1 gradients in seawater-$\varepsilon_{Nd}$ are distinctly different between the EMS and WMS, resulting in a stepwise trend separated by the Strait of Sicily (Fig. 3).

In the WMS, only invariant changes are observed over the past 20 kyr ($\varepsilon_{Nd}$: $-10$ to $-8.5$; Fig. 4). This reflects the predominance of the Atlantic-derived signature for the western WMS in particular, with minor EMS contributions irrespective of water-depth and age. Small variability of the WMS-wide $\varepsilon_{Nd}$ over the Holocene is consistently observed for all records, except for that of shallow-water site RECORD23 (Jiménez-Espejo et al., 2015; Dubois-Dauphin et al., 2017) (Fig. 4).

Comparing sites RECORD23 (414 m depth) located at the easternmost WMS and BP15 (665 m depth) from the EMS suggests a linkage across the Strait of Sicily during the S1-period (Figs. 1–3). Such interaction is revealed by the progressively developing, LIW-related $\varepsilon_{Nd}$ values from BP15 via RECORD23 data-points towards those in the westernmost WMS (Fig. 3). Exchange for the upper waters alone is in agreement with a shallower interface between the MAW and LIW and stagnation of the deeper water masses in the EMS (Fig. 2b). This inference corresponds with a weakening of the anti-estuarine circulation cell with convection depths down to 200–450 m at most, i.e. approximately the base of the LIW (Kallel et al., 1997; Myers et al., 1998; Rohling and De Rijk, 1999; Stratford et al., 2000; Bianchi et al., 2006).

Furthermore, the RECORD23 record displays $\varepsilon_{Nd}$ values of $\sim-8.5$ to $-7.5$ within the S1a phase, but with more radiogenic values ($\sim-8$ to $-6$) for the arid, late-Holocene interval (Fig. 4). These changes have been suggested to reflect a replacement of intermediate waters (Dubois-Dauphin et al., 2017), or an increased inflow of Atlantic waters (Grimm et al., 2015) during the S1-period. In view of our findings and discussion above, this seems rather to be related to variability of the LIW flowing from the EMS to WMS. Due to surface-water freshening in the EMS, the LIW sinking into the WMS may have been shallower during S1 than at present, associated with a shift of intermediate- and deep-water formation to the Ionian Sea (Emeis et al., 2000). In fact, the lack of change in $\varepsilon_{Nd}$ signature during S1-equivalent age for all other WMS records is in line with a smaller LIW inflow, an accordingly smaller Atlantic inflow, and a relatively similar WMS circulation as today.

## 5. Conclusions

Based on the seawater-$\varepsilon_{Nd}$ data – a direct water-mass properties proxy – we provide unequivocal evidence for a severe EMS deep-water stagnation below $\sim$800 m depth. Enhanced Nile runoff and associated preconditioning of deep-water stagnation appear to start up (at least 1 kyr) prior to S1 formation. This stagnation persisted during S1 formation, and terminated synchronously with a basin-wide, deep-water renewal at the end of S1 formation.

The more radiogenic and homogeneous $\varepsilon_{Nd}$ signatures observed for the S1-period can be most-adequately attributed to a 2-fold intensified Nile discharge and a 50% (40–65%) reduced EMS–WMS water exchange. The reduction corresponds to a decreased EMS inflow, and a decreased outflow from the EMS at shallower depths than at present. All evidence together indicates diminished formation of intermediate water, and strongly reduced or even ceased formation of deep water in the EMS. This is consistent with a sluggish and shallower circulation, and thus a longer residence time for EMS seawater during the S1-period ($140 \pm 40$ yr). Conversely, the WMS circulation must have persistently functioned.

This contrasting EMS–WMS circulation dynamics may result from different controls on deep-water formation between the two basins (Rohling et al., 2015). The continued deep-water ventilation, i.e. oxygenation in the WMS but not in the EMS, is in line with sapropel formation in the latter but not in the former. This supports the vision that deep-water stagnation is a prerequisite for sapropel formation.

## Acknowledgements

Many thanks are given to Martina Schulz for sample preparation and chromatography at ICBM. Amalia Filippidi is thanked for laboratory assistance at Utrecht. Qiong Wu and Meng Wang are thanked for the helpful discussion on Nd extraction and box modeling at Tongji, respectively. We thank the captain & crew, scientists, and technicians on board the RVs' cruises for core collection: *Tyro* 1987 & 1993, *Bannock* 1988, *Marion Dufresne* 1991 & 1994/5, *Urania* 1998, *Logachev* 1999, and *Pelagia* 2001 & 2011. Financial supports from the National Natural Science Foundation of China (41806064), China Postdoctoral Science Foundation (2018M640418), and from the EU-projects MARFLUX (MAST1-90022C), PALEOFLUX (MAS2-CT93-0051) & SAP (MAS3-CT97-0137) are acknowledged. We also appreciate the shiptime and logistics granted by CNR and NWO. We are grateful for the critical but constructive comments given by four anonymous reviewers and the editor, that all were very useful to improve our initial manuscripts. This study is part of JW's PhD project, funded by the CSC–UU PhD Program (CSC No. 201206260116; USES contribution 146).

## Appendix A. Supplementary material

Supplementary material related to this article can be found online at https://doi.org/10.1016/j.epsl.2019.01.036.

## References

Ayache, M., Dutay, J.-C., Arsouze, T., Révillon, S., Beuvier, J., Jeandel, J., 2016. High resolution neodymium characterization along the Mediterranean margins and modeling of $\varepsilon_{Nd}$ distribution in the Mediterranean basins. Biogeosciences 13, 5259–5276.

Bayon, G., Dupre, S., Ponzevera, E., Etoubleau, J., Cheron, S., Pierre, C., Mascle, J., Boetius, A., De Lange, G.J., 2013. Formation of carbonate chimneys in the Mediterranean Sea linked to deep-water oxygen depletion. Nat. Geosci. 6, 755–760.

Bianchi, D., Zavatarelli, M., Pinardi, N., Capozzi, R., Capotondi, L., Corselli, C., Masina, S., 2006. Simulations of ecosystem response during the sapropel S1 deposition event. Palaeogeogr. Palaeoclimatol. Palaeoecol. 235, 265–287.

Blaser, P., Lippold, J., Gutjahr, M., Frank, N., Link, J.M., Frank, M., 2016. Extracting foraminiferal seawater Nd isotope signatures from bulk deep sea sediment by chemical leaching. Chem. Geol. 439, 189–204.

Cornuault, M., Tachikawa, K., Vidal, L., Guihou, A., Siani, G., Deschamps, P., Bassinot, F., Revel, M., 2018. Circulation changes in the Eastern Mediterranean Sea over the past 23,000 years inferred from authigenic Nd isotopic ratios. Paleoceanogr. Paleoclimatol. 33. https://doi.org/10.1002/2017PA003227.

De Lange, G.J., Thomson, J., Reitz, A., Slomp, C.P., Principato, M.S., Erba, E., Corselli, C., 2008. Synchronous basin-wide formation and redox-controlled preservation of a Mediterranean sapropel. Nat. Geosci. 1, 606–610.

Dubois-Dauphin, Q., Montagna, P., Siani, G., Douville, E., Wienberg, C., Hebbeln, D., Liu, Z., Kallel, N., Dapoigny, A., Revel, M., Pons-Branchu, E., Taviani, M., Colin, C.,

2017. Hydrological variations of the intermediate water masses of the western Mediterranean Sea during the past 20 ka inferred from neodymium isotopic composition in foraminifera and cold-water corals. Clim. Past 13, 17–37.

Emeis, K.C., Struck, U., Schulz, H.M., Rosenberg, R., Bernasconi, S., Erlenkeuser, H., Sakamoto, T., Martinez-Ruiz, F., 2000. Temperature and salinity variations of Mediterranean Sea surface waters over the last 16,000 years from records of planktonic stable oxygen isotopes and alkenone unsaturation ratios. Palaeogeogr. Palaeoclimatol. Palaeoecol. 158, 259–280.

Filippidi, A., Triantaphyllou, M.V., De Lange, G.J., 2016. Eastern-Mediterranean ventilation variability during sapropel S1 formation, evaluated at two sites influenced by deep-water formation from Adriatic and Aegean Seas. Quat. Sci. Rev. 144, 95–106.

Freydier, R., Michard, A., De Lange, G.J., Thomson, J., 2001. Nd isotopic compositions of Eastern Mediterranean sediments: tracers of the Nile influence during sapropel S1 formation? Mar. Geol. 177, 45–62.

Frost, C.D., O'Nions, R.K., Goldstein, S.L., 1986. Mass balance for Nd in the Mediterranean Sea. Chem. Geol. 55, 45–50.

Gourlan, A.T., Meynadier, L., Allegre, C.J., 2008. Tectonically driven changes in the Indian Ocean circulation over the last 25 Ma: neodymium isotope evidence. Earth Planet. Sci. Lett. 267, 353–364.

Gourlan, A.T., Meynadier, L., Allegre, C.J., Tapponnier, P., Birck, J.L., Joron, J.L., 2010. Northern Hemisphere climate control of the Bengali rivers discharge during the past 4 Ma. Quat. Sci. Rev. 29, 2484–2498.

Grimm, R., Maier-Reimer, E., Mikolajewicz, U., Schmiedl, G., Muller-Navarra, K., Adloff, F., Grant, K.M., Ziegler, M., Lourens, L.J., Emeis, K.C., 2015. Late glacial initiation of Holocene eastern Mediterranean sapropel formation. Nat. Commun. 6, 7099. https://doi.org/10.1038/ncomms8099.

Hennekam, R., Jilbert, T., Schnetger, B., De Lange, G.J., 2014. Solar forcing of Nile discharge and sapropel S1 formation in the early to middle Holocene eastern Mediterranean. Paleoceanography 29, 343–356.

Hennekam, R., Donders, T., Zwiep, K., de Lange, G., 2015. Integral view of Holocene precipitation and vegetation changes in the Nile catchment area as inferred from its delta sediments. Quat. Sci. Rev. 130, 189–199.

Henry, F., Jeandel, C., Dupre, B., Minster, J.F., 1994. Particulate and dissolved Nd in the western Mediterranean Sea: sources, fate and budget. Mar. Chem. 45, 283–305.

Horikawa, K., Martin, E.E., Asahara, Y., Sagawa, T., 2011. Limits on conservative behavior of Nd isotopes in seawater assessed from analysis of fish teeth from Pacific core tops. Earth Planet. Sci. Lett. 310, 119–130.

Jacobsen, S.B., Wasserburg, G.J., 1980. Sm–Nd isotopic evolution of chondrites. Earth Planet. Sci. Lett. 50, 139–155.

Jilbert, T., Reichart, G.J., Mason, P., De Lange, G.J., 2010. Short-time-scale variability in ventilation and export productivity during the formation of Mediterranean sapropel S1. Paleoceanography 25, PA4232. https://doi.org/10.1029/2010PA001955.

Jiménez-Espejo, F.J., Pardos-Gene, M., Martinez-Ruiz, F., Garcia-Alix, A., van de Flierdt, T., Toyofuku, T., Bahr, A., Kreissig, K., 2015. Geochemical evidence for intermediate water circulation in the westernmost Mediterranean over the last 20 kyr BP and its impact on the Mediterranean Outflow. Glob. Planet. Change 135, 38–46.

Kallel, N., Paterne, M., Duplessy, J.C., Vergnaud-Grazzini, C., Pujol, C., Labeyrie, L., Arnold, M., Fontugne, M., Pierre, C., 1997. Enhanced rainfall in the Mediterranean region during the last sapropel event. Oceanol. Acta 20, 697–712.

Kraal, P., Slomp, C.P., De Lange, G.J., 2010. Sedimentary organic carbon to phosphorus ratios as a redox proxy in Quaternary records from the Mediterranean. Chem. Geol. 277, 167–177.

Kuhnt, T., Schmiedl, G., Ehrmann, W., Hamann, Y., Andersen, N., 2008. Stable isotopic composition of Holocene benthic foraminifers from the Eastern Mediterranean Sea: past changes in productivity and deep water oxygenation. Palaeogeogr. Palaeoclimatol. Palaeoecol. 268, 106–115.

Lacan, F., Jeandel, C., 2005. Neodymium isotopes as a new tool for quantifying exchange fluxes at the continent–ocean interface. Earth Planet. Sci. Lett. 232, 245–257.

Le Houedec, S., Meynadier, L., Allegre, C.J., 2012. Nd isotope systematics on ODP Sites 756 and 762 sediments reveal major volcanic, oceanic and climatic changes in South Indian Ocean over the last 35 Ma. Earth Planet. Sci. Lett. 327, 29–38.

Le Houedec, S., Meynadier, L., Allegre, C.J., 2016. Seawater Nd isotope variation in the Western Pacific Ocean since 80 Ma (ODP 807, Ontong Java Plateau). Mar. Geol. 380, 138–147.

Martin, E.E., Scher, H.D., 2004. Preservation of seawater Sr and Nd isotopes in fossil fish teeth: bad news and good news. Earth Planet. Sci. Lett. 220, 25–39.

Martin, E.E., Blair, S.W., Kamenov, G.D., Scher, H.D., Bourbon, E., Basak, C., Newkirk, D.N., 2010. Extraction of Nd isotopes from bulk deep sea sediments for paleoceanographic studies on Cenozoic time scales. Chem. Geol. 269, 414–431.

Matthews, A., Azrieli-Tal, I., Benkovitz, A., Bar-Matthews, M., Vance, D., Poulton, S.W., Teutsch, N., Almogi-Labin, A., Archer, C., 2017. Anoxic development of sapropel S1 in the Nile Fan inferred from redox sensitive proxies, Fe speciation, Fe and Mo isotopes. Chem. Geol. 475, 24–39.

Myers, P.G., Haines, K., Rohling, E.J., 1998. Modeling the paleocirculation of the Mediterranean: the last glacial maximum and the Holocene with emphasis on the formation of sapropel S-1. Paleoceanography 13, 586–606.

Myers, P.G., 2002. Flux-forced simulations of the paleocirculation of the Mediterranean. Paleoceanography 17, 1009. https://doi.org/10.1029/2000PA000613.

Osborne, A.H., Marino, G., Vance, D., Rohling, E.J., 2010. Eastern Mediterranean surface water Nd during Eemian sapropel S5: monitoring northerly (mid-latitude) versus southerly (sub-tropical) freshwater contributions. Quat. Sci. Rev. 29, 2473–2483.

Pinardi, N., Masetti, E., 2000. Variability of the large scale general circulation of the Mediterranean Sea from observations and modelling: a review. Palaeogeogr. Palaeoclimatol. Palaeoecol. 158, 153–174.

Revel, M., Ducassou, E., Skonieczny, C., Colin, C., Bastian, L., Bosch, D., Migeon, S., Mascle, J., 2015. 20,000 years of Nile River dynamics and environmental changes in the Nile catchment area as inferred from Nile upper continental slope sediments. Quat. Sci. Rev. 130, 200–221.

Roberts, N.L., Piotrowski, A.M., Elderfield, H., Eglinton, T.I., Lomas, M.W., 2012. Rare earth element association with foraminifera. Geochim. Cosmochim. Acta 94, 57–71.

Roether, W., Manca, B.B., Klein, B., Bregant, D., Georgopoulos, D., Beitzel, V., Kovacevic, V., Luchetta, A., 1996. Recent changes in eastern Mediterranean deep waters. Science 271, 333–335.

Rohling, E.J., 1994. Review and new aspects concerning the formation of Eastern Mediterranean sapropels. Mar. Geol. 122, 1–28.

Rohling, E.J., De Rijk, S., 1999. Holocene climate optimum and last glacial maximum in the Mediterranean: the marine oxygen isotope record. Mar. Geol. 161, 385–387.

Rohling, E.J., Marino, G., Grant, K.M., 2015. Mediterranean climate and oceanography, and the periodic development of anoxic events (sapropels). Earth-Sci. Rev. 143, 62–97.

Rossignol-Strick, M., 1983. African monsoons, an immediate climate response to orbital insolation. Nature 304, 46–49.

Schenau, S.J., De Lange, G.J., 2000. A novel chemical method to quantify fish debris in marine sediments. Limnol. Oceanogr. 45, 963–971.

Scheuvens, D., Schutz, L., Kandler, K., Ebert, M., Weinbruch, S., 2013. Bulk composition of northern African dust and its source sediments – a compilation. Earth-Sci. Rev. 116, 170–194.

Schmiedl, G., Kuhnt, T., Ehrmann, W., Emeis, K.C., Hamann, Y., Kotthoff, U., Dulski, P., Pross, J., 2010. Climatic forcing of eastern Mediterranean deep-water formation and benthic ecosystems during the past 22,000 years. Quat. Sci. Rev. 29, 3006–3020.

Scrivner, A.E., Vance, D., Rohling, E.J., 2004. New neodymium isotope data quantify Nile involvement in Mediterranean anoxic episodes. Geology 32, 565–568.

Siddall, M., Khatiwala, S., van de Flierdt, T., Jones, K., Goldstein, S.L., Hemming, S., Anderson, R.F., 2008. Towards explaining the Nd paradox using reversible scavenging in an ocean general circulation model. Earth Planet. Sci. Lett. 274, 448–461.

Slomp, C.P., Thomson, J., De Lange, G.J., 2002. Enhanced regeneration of phosphorus during formation of the most recent eastern Mediterranean sapropel (S1). Geochim. Cosmochim. Acta 66, 1171–1184.

Spivack, A.J., Wasserburg, G., 1988. Neodymium isotopic composition of the Mediterranean outflow and the eastern North Atlantic. Geochim. Cosmochim. Acta 52, 2767–2773.

Stratford, K., Williams, R.G., Myers, P.G., 2000. Impact of the circulation on sapropel formation in the eastern Mediterranean. Glob. Biogeochem. Cycles 14, 683–695.

Tachikawa, K., Roy-Barman, M., Michard, A., Thouron, D., Yeghicheyan, D., Jeandel, C., 2004. Neodymium isotopes in the Mediterranean Sea: comparison between seawater and sediment signals. Geochim. Cosmochim. Acta 68, 3095–3106.

Tachikawa, K., Piotrowski, A., Bayon, G., 2014. Neodymium associated with foraminiferal carbonate as a recorder of seawater isotopic signatures. Quat. Sci. Rev. 88, 1–13.

Tachikawa, K., Vidal, L., Cornuault, M., Garcia, M., Pothin, A., Sonzogni, C., Bard, E., Menot, G., Revel, M., 2015. Eastern Mediterranean Sea circulation inferred from the conditions of S1 sapropel deposition. Clim. Past 11, 855–867.

Tachikawa, K., Arsouze, T., Bayon, G., Bory, A., Colin, C., Dutay, J., Frank, N., Giraud, X., Gourlan, A.T., Jeandel, C., Lacan, F., Meynadier, L., Montagna, P., Piotrowski, A.M., Plancherel, Y., Pucéat, E., Roy-Barman, M., Waelbroeck, C., 2017. The large-scale evolution of neodymium isotopic composition in the global modern and Holocene ocean revealed from seawater and archive data. Chem. Geol. 457, 131–148.

Tanaka, T., Togashi, S., Kamioka, H., Amakawa, H., Kagami, H., Hamamoto, T., Yuhara, M., Orihashi, Y., Yoneda, S., Shimizu, H., Kunimaru, T., Takahashi, K., Yanagi, T., Nakano, T., Fujimaki, H., Shinjo, R., Asahara, Y., Tanimizu, M., Dragusanu, C., 2000. JNdi-1: a neodymium isotopic reference in consistency with LaJolla neodymium. Chem. Geol. 168, 279–281.

Tesi, T., Asioli, A., Minisini, D., Maselli, V., Valle, G.D., Gamberi, F., Langone, L., Cattaneo, A., Montagna, P., Trincardi, F., 2017. Large-scale response of the Eastern Mediterranean thermohaline circulation to African monsoon intensification during sapropel S1 formation. Quat. Sci. Rev. 159, 139–154.

Thunell, R.C., Williams, D.F., 1989. Glacial-Holocene salinity changes in the Mediterranean Sea – hydrographic and depositional effects. Nature 338, 493–496.

Vance, D., Scrivner, A.E., Beney, P., Staubwasser, M., Henderson, G.M., Slowey, N.C., 2004. The use of foraminifera as a record of the past neodymium isotope composition of seawater. Paleoceanography 19, PA2009. https://doi.org/10.1029/2003PA000957.

Wilson, D.J., Piotrowski, A.M., Galy, A., Clegg, J.A., 2013. Reactivity of neodymium carriers in deep sea sediments: implications for boundary exchange and paleoceanography. Geochim. Cosmochim. Acta 109, 197–221.

Wu, J., Böning, P., Pahnke, K., Tachikawa, K., De Lange, G.J., 2016. Unraveling North-African riverine and eolian contributions to central Mediterranean sediments during Holocene sapropel S1 formation. Quat. Sci. Rev. 152, 31–48.

Wu, J., Liu, Z., Stuut, J.-B., Zhao, Y., Schirone, A., De Lange, G.J., 2017. North-African paleodrainage discharges to the central Mediterranean during the last 18,000 years: a multiproxy characterization. Quat. Sci. Rev. 163, 95–113.

Wu, Q., Colin, C., Liu, Z.F., Thil, F., Dubois-Dauphin, Q., Frank, N., Tachikawa, K., Bordier, L., Douville, E., 2015. Neodymium isotopic composition in foraminifera and authigenic phases of the South China Sea sediments: implications for the hydrology of the North Pacific Ocean over the past 25 kyr. Geochem. Geophys. Geosyst. 16, 3883–3904.

Ziegler, M., Tuenter, E., Lourens, L.J., 2010. The precession phase of the boreal summer monsoon as viewed from the eastern Mediterranean (ODP Site 968). Quat. Sci. Rev. 29, 1481–1490.